J|A|C|S

Structure-Directing Behaviors of Tetraethylammonium Cations toward Zeolite Beta Revealed by the Evolution of Aluminosilicate Species Formed during the Crystallization Process

Takaaki Ikuno,[†,¶] Watcharop Chaikittisilp,[†,¶] Zhendong Liu,[†] Takayuki Iida,[†] Yutaka Yanaba,[‡] Takeshi Yoshikawa,[‡] Shinji Kohara,[§,#] Toru Wakihara,[†] and Tatsuya Okubo*[,†]

[†]Department of Chemical System Engineering, The University of Tokyo, 7-3-1 Hongo, Bunkyo-ku, Tokyo 113-8656, Japan
[‡]Institute of Industrial Science, The University of Tokyo, 4-6-1 Komaba, Meguro-ku, Tokyo 153-8505, Japan
[§]Research and Utilization Division, Japan Synchrotron Radiation Research Institute, 1-1-1 Kouto, Sayo-cho, Sayo, Hyogo 679-5198, Japan

Ⓢ *Supporting Information*

ABSTRACT: Organic structure-directing agents (OSDAs) have been widely used for the synthesis of zeolites. In most cases, OSDAs are occluded in zeolites as an isolated cation or molecule geometrically fitted within the zeolite cavities. This is not the case for zeolite beta synthesized by using tetraethylammonium (TEA$^+$) cation as an OSDA, in which a cluster/aggregate of ca. six TEA$^+$ cations is occluded intact in the cavity (i.e., the channel intersection) of zeolite beta. The structure direction of TEA$^+$ in such a nontypical, clustered mode has remained elusive. Here, zeolite beta was hydrothermally synthesized using TEA$^+$ in the absence of other alkali metal cations in order to focus on the structure-directing behaviors of TEA$^+$ alone. The solid products formed throughout the hydrothermal synthesis were analyzed by an array of characterization techniques including argon adsorption−desorption, high-energy X-ray total scattering, Raman and solid-state NMR spectroscopy, and high-resolution transmission electron microscopy. It was revealed that the formation of amorphous TEA$^+$−aluminosilicate composites and their structural, chemical, and textural evolution toward the amorphous zeolite beta-like structure during the induction period is vital for the formation of zeolite beta. A comprehensive scheme of the formation of zeolite beta is proposed paying attention to the clustered behavior of TEA$^+$ as follows: (i) the formation of the TEA$^+$−aluminosilicate composites after heating, (ii) the reorganization of aluminosilicates together with the conformational rearrangement of TEA$^+$, yielding the formation of the amorphous TEA$^+$−aluminosilicate composites with the zeolite beta-like structure, (iii) the formation of zeolite beta nuclei by solid-state reorganization of such zeolite beta-like, TEA$^+$−aluminosilicate composites, and (iv) the subsequent crystal growth. It is anticipated that these findings can provide a basis for broadening the utilization of OSDAs in the clustered mode of structure direction in more effective ways.
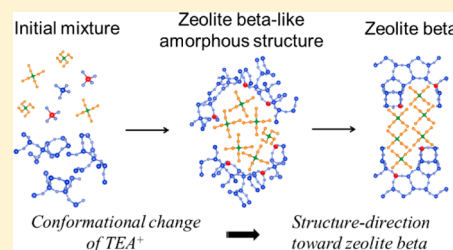
INTRODUCTION

Understanding the formation mechanisms of industrially important materials is of great scientific and technological significance, as it can provide a critical basis to control their physicochemical properties and functions, thereby improving the performances of the materials. Zeolites, a series of microporous crystalline aluminosilicates, are one of the key materials utilized in a number of real applications across several industries due to their unique crystalline structures, molecular-sized pores and cavities, and their several intrinsic properties arising from their anionic frameworks.[1−6] The formation mechanisms of zeolites have not been fully clarified yet because zeolites are formed through an intricate sequence of chemical reactions under hydrothermal conditions, although several studies have made the mechanisms more clear than before.[7−30]

Organic structure-directing agents (OSDAs) have often been used for the synthesis of zeolites, especially with high silicon-to-aluminum ratios.[31,32] In addition, many zeolites possessing unconvent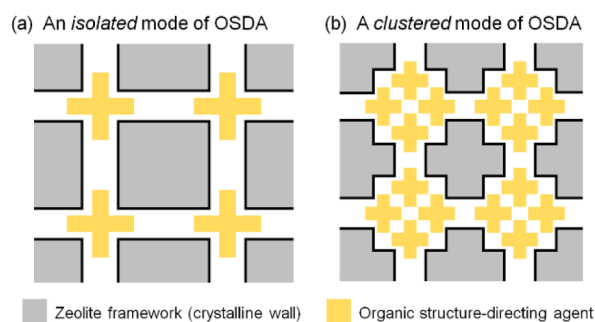ional chemical compositions and/or new structures have been formed only by using several specified OSDAs.[33] Such OSDAs are typically occluded in the zeolite cavities as an isolated cation or molecule, with the representative example being the tetrapropylammonium (TPA$^+$) cation located at the channel intersection of MFI zeolite.[34] The structure direction of such OSDAs has been explained in terms of a geometric fit between isolated OSDAs and zeolite cavities,[31−33] leading to maximized stabilization energy that, in the case of siliceous zeolites, can sometimes be predicted computationally.[35−37] However, since the formation of (alumino)silicate zeolites is so complex and controlled kinetically, the most stable crystalline phase does not need to be formed. The elucidation of the structure direction of OSDAs can thus contribute to the rational and systematic search for zeolites with unique structures and/or extralarge pores.[33]

Siliceous MFI zeolite (silicalite-1) synthesized using TPA$^+$ has been a model system for the mechanistic studies of zeolite formation.[7–9,14–23] At the molecular level, solid-state nuclear magnetic resonance (NMR) spectroscopic studies have suggested that the key initial step for the structure direction of TPA$^+$ is the formation of TPA$^+$–silicate composite species, as primary units, in which the hydrophobic hydration sphere formed around TPA$^+$ is replaced by silicate species.[14–16] This process has been thought to be driven by the van der Waals interactions between silicate species and alkyl chains of TPA$^+$ (enthalpic effects) as well as by the release of water molecules from the hydrophobic hydration sphere into bulk water (entropic effects). Further investigations have revealed evidence that the nucleation of silicalite-1 proceeds through the aggregation of the primary units, yielding primary nano-particles,[17,18] followed by the subsequent restructuring of such primary nanoparticles.[7,8,22] In a crystal growth step, very recently, in situ imaging by atomic force microscopy (AFM) has provided direct evidence that silicalite-1 crystals are grown by both the attachment of nanoparticle precursors to the crystal surface followed by structural rearrangement and the gradual addition of molecular silicate species.[9]

Unlike *an isolated mode* of the structure direction of TPA$^+$ for MFI zeolite, the formation of zeolite beta (*BEA-type zeolite) seems to be directed by a cluster/aggregate of tetraethylammonium (TEA$^+$) cations as an OSDA,[25] termed here as *a clustered mode* of the structure direction (Figure 1). As is previously

(a) An *isolated* mode of OSDA   (b) A *clustered* mode of OSDA

☐ Zeolite framework (crystalline wall)   ▨ Organic structure-directing agent

Figure 1. Schematics of the structure direction in (a) isolated and (b) clustered modes.

known, six TEA$^+$ cations, together with inorganic cations, if any, are always occluded intact in zeolite beta, having up to about seven Al/unit cell (calculated based on a unit cell of *BEA framework consisting of 64 tetrahedral atoms), irrelevant to the synthesis methods and conditions.[24,25,38] Considering the structure and channel dimensions (5.6 × 5.6 and 6.6 × 6.7 Å^2) of the *BEA framework, six TEA$^+$ cations (the size of TEA$^+$ is ca. 7.0–7.4 Å, depending on its molecular conformation) cannot be isolatedly occluded in the zeolite framework. Instead, it has been suggested that six such TEA$^+$ are present together in a nonisolated manner in the microporous cavity (i.e., the channel intersection) of zeolite beta.[25] The presence of an OSDA in such a nonisolated manner has also been observed in other zeolites; for example, two TEA$^+$ cations have been suggested to be occluded in the *lta*-cage cavity of UZM-5 zeolite.[39]

The formation mechanisms of zeolite beta have been described to be similar to those of silicalite-1, wherein the primary nanoparticles aggregate with simultaneous migration of TEA$^+$ and incorporation of aluminum to form secondary aluminosilicate nanoparticles. As the surface charges of such

secondary nanoparticles decrease, thereby becoming colloidally less stable, the tertiary nanoparticles, identified as zeolite beta, are then formed by the aggregation of the secondary nanoparticles.[27–29] Although the nucleation event is still unclear, viable nuclei of zeolite beta may be formed by the oriented aggregation of the secondary nanoparticles possessing a zeolite beta-like microstructure,[7,8] the reorganization at the solid–liquid interface where the secondary nanoparticles attach to each other,[10,11] or a combination of both.

On the basis of the previous studies on zeolite formation, mainly in clear solutions,[7–9,12,17–23,27–30] the growth of zeolites seems to generally occur via the aggregation of nanoparticle precursors. However, this mechanism is not necessarily valid for the more dense, hydrogel system, typically used in industry for large-scale production of zeolites.[3,4] In addition, the exact microstructure of nanoparticle precursors and the molecular-level understanding of the structure direction of organic cations/molecules, particularly in the clustered mode, are still elusive.[9]

We report herein a clearer comprehensive scheme of the formation of zeolite beta synthesized from a dense, hydrogel system by using TEA$^+$ as the OSDA. In particular, we follow the structural, chemical, and textural evolution of TEA$^+$–aluminosilicate species formed during the crystallization of zeolite beta with a special focus on the clustered behavior of TEA$^+$ by a battery of characterization techniques. The crucial step for the formation of zeolite beta likely lies in the induction period, where the amorphous TEA$^+$–aluminosilicate species are gradually transformed into the zeolite beta-like structure, induced by the clustering and conformational change of TEA$^+$. This conformational change of TEA$^+$ clusters results in the structure direction of TEA$^+$ toward zeolite beta.

■ EXPERIMENTAL SECTION

Zeolite Synthesis. Zeolite beta was synthesized according to the previously reported conditions[38] with some modification. The starting mixture was prepared with a molar composition of 1.0 SiO$_2$:0.025 Al$_2$O$_3$:0.5 TEAOH:16 H$_2$O. Typically, aluminum hydroxide (Wako Pure Chemical Industries) was dissolved in an aqueous solution of tetraethylammonium hydroxide (TEAOH, 35 wt %, Sigma-Aldrich) by heating the mixture at 80 °C overnight. After the solution was cooled to room temperature, a proper amount of distilled water was added. Then, fumed silica (Cab-O-Sil M5, Cabot) was added slowly under stirring, and the resultant mixture was stirred for another 15 min. This synthesis mixture was loaded to a 23 mL Teflon-lined stainless steel autoclave. The sealed autoclave was heated at 140 °C under static conditions in a preheated air-circulated oven. The hydrothermal synthesis time was varied between 0 and 240 h. After the prescribed synthesis time, the autoclave was removed from the oven and quenched with cool tap water. Solid products were recovered by centrifugation and subsequently washed with distilled water until the filtrate had an approximately neutral pH. Recovered products were dried at 80 °C overnight before further characterizations.

Synthesis of zeolite beta by intermediate addition of zeolite beta crystals as seeds into the hydrothermally treated synthesis mixture was also carried out. Following the procedure described above, the starting mixture was hydrothermally treated for 24 or 72 h and then quenched and cooled to room temperature. To the treated product were added the as-synthesized zeolite beta crystals (synthesized for 240 h; 5 wt % based on silica). After being blended by a planetary centrifugal mixer (Thinky ARE-310) at 2000 rpm for 30 s twice, the resultant mixture was then loaded in a stainless steel tubular reactor[40] and heated at 140 °C for 1–5 h in a preheated oil bath. Solid products were collected and washed as described above.

Characterization. Powder X-ray diffraction (XRD) patterns were recorded on an Ultima IV diffractometer (Rigaku) using Cu Kα

radiation with a D/Tex Ultra detector. High-energy X-ray total scattering (HEXTS) measurements were conducted at the beamline BL04B2 (SPring-8, Japan) with a horizontal two-axis diffractometer, dedicated to glass and liquid amorphous materials. The powder sample was stuffed in a quartz capillary with an alumina ball and vacuum grease on top. The incident photon energy was 61.43 keV (λ = 0.2018 Å). The maximum Q ($Q = 4\pi \sin \theta/\lambda$; θ is scattering angle, λ is the wavelength of the photons), Q_{max}, collected in this study was 25 Å^{-1}.[41] The obtained data were subjected to well-established analysis procedures, such as absorption, background, and Compton scattering corrections, and then normalized to give the Faber–Ziman total structure factor, $S(Q)$.[42,43] Then, the pair distribution function, $G(r)$, was calculated from $S(Q)$ by using the following equation:

$$G(r) = 4\pi r[\rho(r) - \rho_0] = \frac{2}{\pi} \int_{Q\,min}^{Q\,max} Q[S(Q) - 1] \sin(Qr)\,dQ$$

where ρ_0 is the atomic number density (0.06021/Å^3, 53Si:5Al:116O, 1.53 g cm^{-3}).

Fourier transform infrared (FT-IR) spectra were recorded on an FT-IR 6100 (JASCO) spectrometer using the KBr method. Solid-state magic-angle-spinning (MAS) NMR experiments were conducted on a JNM-ECA 500 (JEOL). ^{27}Al MAS NMR spectra were recorded at 130.33 MHz with a $\pi/2$ pulse length of 3.2 μs, a recycle delay of 5 s, and a spinning frequency of 14 kHz. ^{29}Si MAS NMR spectra were recorded at 99.37 MHz with a $\pi/2$ pulse length of 5.0 μs, a recycle delay of 60 s, and a spinning frequency of 10 kHz. Raman spectra of the solid products were collected on an NRS-5100 (JASCO) by using a laser of 532 nm. CHN elemental analyses were performed on a CE-440 elemental analyzer (Exeter Analytical). The amounts of silicon and aluminum in the products were quantified on an inductively coupled plasma–atomic emission spectrometer (ICP-AES) (iCAP-6300, Thermo Scientific). Thermogravimetric and differential thermal analyses (TG-DTA) were performed on a PU 4K (Rigaku) from 30 to 800 °C at a heating rate of 10 K min^{-1} under a flow (200 mL min^{-1}) of 10% O$_2$/90% He mixed gas. Argon adsorption–desorption measurements were conducted at −186 °C on an Autosorb-iQ2-MP (Quantachrome Instruments). Prior to the measurement, the sample was calcined under the condition described in Figure S1 in the Supporting Information (SI), which was decided based on the TGA measurements to ensure the complete removal of TEA$^+$, and then outgassed at 400 °C under high vacuum. Pore size distribution and micropore volume were calculated by the nonlocal density functional theory (NLDFT), assuming argon adsorption in cylindrical siliceous zeolite pores in the micropore range and in cylindrical pores of amorphous silica in the mesopore range.[44] Field-emission scanning electron microscopy (FE-SEM) images were obtained with a JSM-7500FA (JEOL). Transmission electron microscopy (TEM) observations were carried out on a JEM-200EX-II (JEOL) at an accelerating voltage of 200 kV.

■ RESULTS AND DISCUSSION

Structural Evolution. As reported previously, the presence of alkali metal cations such as Na$^+$ in the synthesis of zeolite beta can affect crystalline phase selectivity, nucleation and crystal growth rates, and crystal morphology.[29,38,45] For a better understanding of the structure direction of TEA$^+$, zeolite beta was synthesized under hydrothermal conditions from alkali metal cation-free mixtures to avoid any influences of alkali cations.[38] Figure 2a shows powder XRD patterns of the products collected after hydrothermal treatment for different periods of time. A notable change was first observed after 24 h of hydrothermal treatment. The appearance of a broad peak at 2θ = 7.6°, which is also seen for highly crystalline zeolite beta, likely suggests the formation of certain periodic structures.[46] Upon heating, a broad hump at 2θ = 20–25°, a characteristic of amorphous (alumino)silicates, shifted toward higher angles (also see Figure S2 in the SI; red arrow), probably due to the
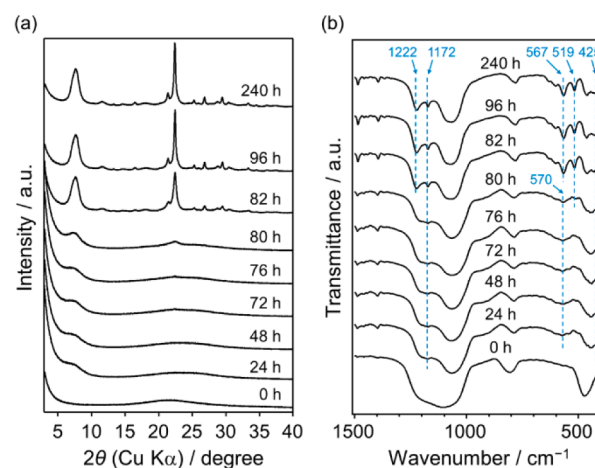

Figure 2. (a) Powder XRD patterns and (b) FT-IR spectra of the products synthesized for different periods of time.

formation of smaller ring structures of aluminosilicates.[47] The induction period continued until about 80 h of hydrothermal treatment, whereupon a noticeable Bragg diffraction peak at 2θ = 22.5° started to appear. During the induction period, the peak intensities of XRD patterns slightly increased as the hydrothermal treatment continued. After 82 h, the intensities of XRD peaks sharply increased, and all peaks can be assigned to zeolite beta. Further increases in the peak intensities with prolonged hydrothermal treatment were observed, suggesting the crystal growth of zeolite beta.

Structural evolution was further investigated by FT-IR spectroscopy. Compared to an FT-IR spectrum of TEA$^+$ (Figure S3 in the SI), FT-IR bands at 425, 1172, and 1300–1500 cm^{-1} observed in the as-synthesized products can be assigned to TEA$^+$ (see Figure 2b), suggesting that TEA$^+$ is occluded in the solid products. After 24 h of heating, a broad band at around 1200 cm^{-1}, assigned to the T–O asymmetric stretch of external linkages,[48] appeared. This band is typically found in zeolites with five-membered-ring (5R) chains,[49] suggesting that the solid products formed after heating contain 5R (alumino)silicates. In addition, a weak broad band at 570 cm^{-1}, assigned to 5R-rich units, namely, 5–5 (containing two parallel faces of nearly planar 5Rs) and 5–3 (having four faces of puckered 5Rs in the envelope mode),[49] was also observed, again suggesting the presence of 5Rs in the hydrothermally heated samples. After the onset of crystallization, the products obtained by hydrothermal treatment for 82–240 h, which are identified as zeolite beta by XRD, showed the characteristic bands of zeolite beta at 519, 567, and 1222 cm^{-1}.[45,50,51]

The shape and size of the solid products were observed by FE-SEM (Figure 3). Note that the particle sizes described here were averaged from more than 100 particles. The product before hydrothermal synthesis (0 h) consisted of nanoparticles of 15–35 nm in diameter with irregular morphology, likely representing the undissolved fumed silica (as a silica source). After 24 h of hydrothermal treatment, aggregates of particles with a primary diameter less than 10 nm were observed. The decrease in particle sizes suggests the dissolution of the starting materials. Only slight increases in particle sizes were observed after further hydrothermal treatment up to 80 h (about 12 nm for the 80 h product). The nanoparticles with an almost constant diameter existing before the appearance of XRD peaks have also been detected previously by scattering techniques in the synthesis of zeolite beta from clear solutions,[27–30,50–52] in
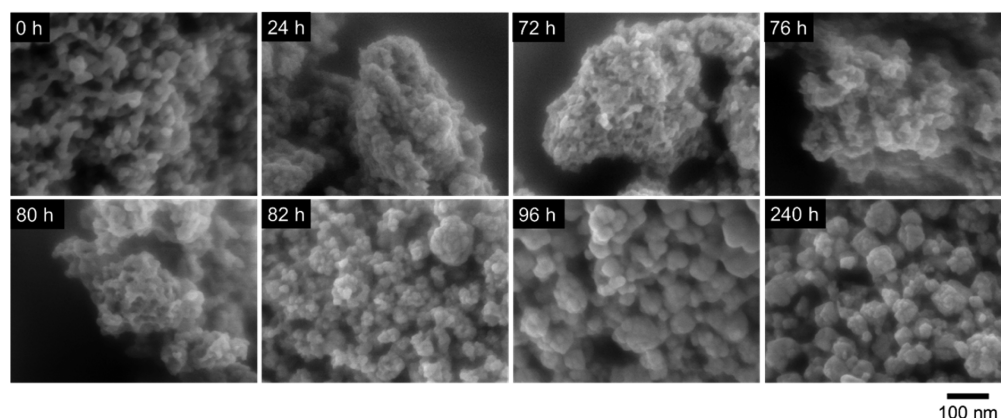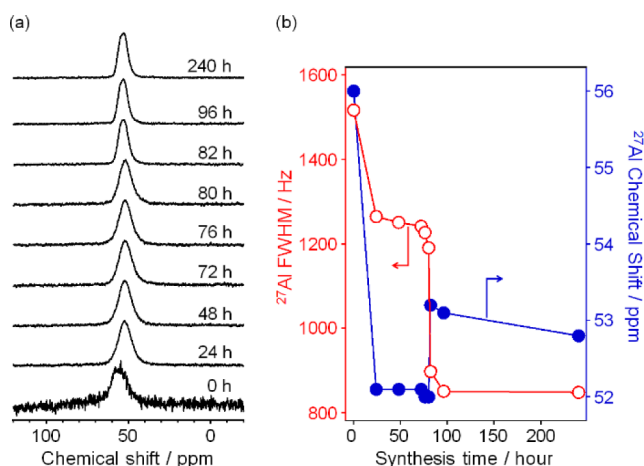
Figure 3. FE-SEM images of the products synthesized for different periods of time.

which the nucleation of zeolite beta has been suggested to occur during the aggregation process of such nanoparticles.[27−30] Even though the first apparent XRD peak was observed for the sample after 80 h of heating, its FE-SEM image was almost identical to those obtained from shorter hydrothermal treatment, suggesting either that zeolite beta nuclei are embedded in amorphous solid or that they are formed by solid-state reorganization of aggregated nanoparticles. After treatment for 82 h, where the XRD pattern corresponding to zeolite beta was obviously observed (Figure 2a), the FE-SEM image revealed the formation of isolated particles with a diameter of 10−25 nm. During this stage, no significant change in particle size was observed, further suggesting that zeolite beta nuclei are likely formed by solid-state reorganization of aluminosilicate particles. Prolonged synthesis resulted in the crystal growth, as particles with larger sizes of 20−60 nm with crystal-like facets were observed after 240 h of hydrothermal treatment.

^{27}Al and ^{29}Si solid-state MAS NMR measurements were conducted to investigate the structural change of aluminosilicates in an atomic scale. As shown in Figure 4a, none of the six-coordinated Al species, generally appearing at a chemical shift (δ) of ca. 0 ppm,[53] were observed throughout the synthesis even in the mixture without heating (0 h), suggesting that most of the aluminum source, if not all, is dissolved during the

preparation of the starting mixture (the used aluminum source does not contain four-coordinated Al). Only one peak was observed, at δ = 52.1−56.0 ppm, corresponding to four-coordinated Al species.[53] It is likely that all dissolved aluminate species reacted with silicates, due to their high affinity for bonding with silicates, and then become aluminosilicates with four-coordinated Al, although it should be mentioned that some NMR-invisible five- or six-coordinated Al species may exist.[53] As is well known, the chemical shift is sensitive to Al−O−Si bond angles.[53,54] The peak shifting from 56.0 to 52.1 ppm by 24 h of heating (see Figure 4b, right axis) indicates an increase in the average Al−O−Si angles. An enhanced signal-to-noise ratio after 24 h likely suggests the increased content of Al in the solid products. The full width at half-maximum (fwhm) of the four-coordinated peaks is plotted in Figure 4b (left axis). The fwhm of the peaks decreased dramatically during the first 24 h of hydrothermal treatment, suggesting that the structure of aluminosilicates becomes more ordered, that is, narrower distributions of Al−O−Si angles. Combined with the XRD, FT-IR, and FE-SEM results described above, during the first 24 h, the dissolved aluminate species seem to react with silicate species, resulting in aluminosilicate species with 5R-rich units. The fwhm decreased slowly during further heating for up to 76 h, suggesting that the structural order of amorphous aluminosilicates is gradually enhanced during this induction period. Upon heating between 76 and 82 h, the observed downfield shift of the NMR peak from 52.1 to 53.2 ppm (see Figure 4b, right axis) indicates a decrease in the average Al−O−Si angles. With the formation of zeolite beta (80−82 h), the fwhm decreased rapidly (see Figure 4b, left axis), evidencing the well-ordered aluminosilicates, that is, zeolite beta crystals.

Figure 5 shows ^{29}Si MAS NMR spectra. The product before heating was rich in Q^4(0Al) silicon species (Si(SiO)$_4$), as the spectrum showed the strongest signal around δ = −110 ppm.[53] Hydrothermal treatment for 24 h caused the dissolution of silica, as evidenced by the signal shift to δ = −100 ppm, assigned to Q^3(0Al) ((SiO)$_3$SiOH or (SiO)$_3$SiO$^-$) or Q^4(2Al) (Si(AlO)$_2$(SiO)$_2$) silicon species. Increases in the signal intensities at about −110 ppm upon hydrothermal treatment up to 76 h indicate the increase in Q^4(0Al) species, suggesting the condensation of silicates during the induction period. This is also in line with ^{27}Al MAS NMR, in which the structural evolution during the induction period was observed. Further hydrothermal treatment up to 82 h resulted in the appearance of a sharp, outstanding peak at −110 ppm together with a shoulder at higher chemical shifts, indicating the enhanced


Figure 4. (a) ^{27}Al MAS NMR spectra and (b) full width at half-maximum (left axis; empty red symbols) and position (right axis; filled blue symbols) of each NMR peak of the products synthesized for different periods of time.
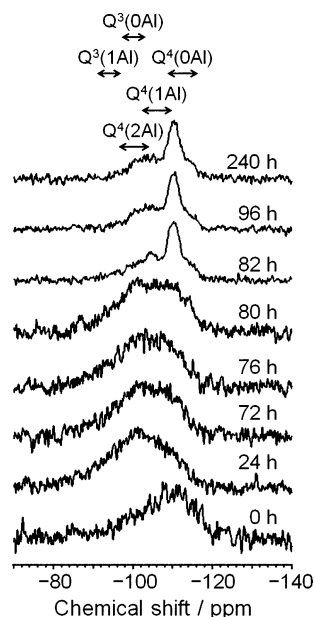
Figure 5. ^{29}Si MAS NMR spectra of the products synthesized for different periods of time.

structural order and condensation of silicates with the formation of zeolite beta.

Structural evolution of aluminosilicates in an intermediate-range order was investigated by HEXTS measurements.[41] Figure S4 in the SI shows the total structural factors, $S(Q)$, of the products after 72 and 96 h of hydrothermal treatment. The $S(Q)$ of the product before the onset of crystallization (72 h) exhibited the oscillation typically observed in amorphous aluminosilicates. On the other hand, the $S(Q)$ of the product after 96 h showed sharp peaks at Q values below 10 Å^{-1}, corresponding to zeolite beta. Figure 6 shows the pair
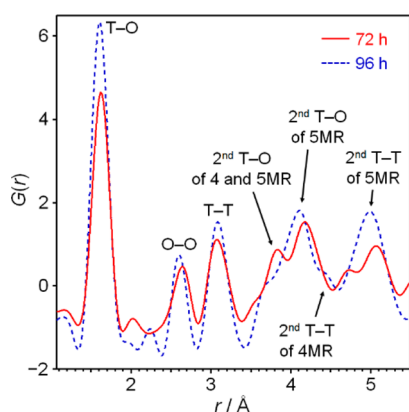
Figure 6. Pair distribution functions, $G(r)$, of the products synthesized for 72 (red, solid line) and 96 h (blue, dashed line).

distribution functions, $G(r)$, of the products. The peaks at 1.6, 2.6, and 3.1 Å correspond to the distances of the first nearest T−O, O−O, and T−T, respectively (T = Si or Al). These three peaks are intrinsically originated from the presence of T and O atoms in aluminosilicates and therefore commonly seen regardless of sizes and structures of aluminosilicate rings.[12,41,47] Comparison of $G(r)$ above 3.5 Å can give us useful information on medium-range structures of aluminosilicates.[41] The peak observed at 3.8 Å is assigned to the second

nearest T−O distances of 4Rs and 5Rs. There are two peaks corresponding mainly to the presence of 5Rs. One was observed between 4.0 and 4.3 Å, assigned to the second nearest T−O distances; the other at 4.8−5.1 Å corresponds to the second nearest T−T distances.

The intensity of the peak at 3.8 Å notably decreased upon the formation of zeolite beta observable by XRD, while the intensities of other main peaks corresponding to 5Rs (at 4.0−4.3 and 4.8−5.1 Å) hardly decreased, indicating the decrease in the fraction of 4Rs. Meanwhile, a peak assigned to the second nearest T−T distance of 4Rs appeared at 4.4 Å after 96 h, indicating its enhanced order. The decrease in the 4R fraction simultaneous with the enhancement in its order was further supported by Raman spectra of the as-synthesized products in a silicate ring region (220−600 cm^{-1})[55] shown in Figure S5 in the SI. Before hydrothermal treatment (0 h), the band seen at 495 cm^{-1} can be assigned to 4Rs in amorphous (alumino)-silicates. After zeolite beta was formed (as detected by powder XRD), the band assigned to 4Rs was shifted to ca. 460 cm^{-1}. These results suggest that the intermediate-range structures of 4Rs in amorphous solids are somehow different from those existing in zeolite beta.

The peaks at 4.0−4.3 and 4.8−5.1 Å, mainly attributed to 5Rs (the second nearest T−O and T−T distances, respectively), shifted toward shorter distance upon prolonged heating from 72 h (XRD amorphous solid) to 96 h (highly crystalline zeolite beta), suggesting that the 5Rs in zeolite beta are more rigid than those in amorphous solid (in other words, the shrinkage of 5Rs takes place). Taking into account that zeolite beta contains a considerable amount of 5Rs (see ring distribution of *BEA-type zeolite in Figure S6 in the SI), these $G(r)$ results agree well with ^{27}Al MAS NMR results, in which the decrease of the average Al−O−Si angles upon the formation of zeolite beta was observed (*vide supra*).

To further investigate the periodicity of the products obtained when the nucleation is assumed to occur, the products after 76 and 82 h of heating were characterized by TEM. Figure 7 shows high-resolution TEM (HR-TEM) images and the corresponding fast Fourier transforms (FFTs) of the selected areas (white frames in HR-TEM images). In Figure 7c, lattice fringes, indicative of crystalline orders, with a distance between lattices measured to be 1.10 nm were observed in the product obtained after 82 h. This value matches well with the XRD peak seen at $2\theta = 7.6°$ (a d-spacing of 1.16 nm). The correspondent pattern is shown in the FFT (Figure 7d). No grain boundary was observed in the HR-TEM image (also see additional images in Figure S7 in the SI), implying that the nucleation of zeolite beta likely proceeds via the solid-state reorganization of aluminosilicate species,[12] not the oriented aggregation.[7,8,22,27]

Very interestingly, the local periodic structure was also observed in an HR-TEM image (Figure 7a) of the XRD-amorphous product obtained after 76 h (see its XRD pattern in Figure 2a). The presence of the local periodic structure was directly evidenced by the appearance of a bright ring pattern in the FFT (Figure 7b). Calculated from a radius of the ring pattern, the period of the structure was 1.10 nm, which is identical to the measured lattice distance in the HR-TEM image of the crystalline product after 82 h of hydrothermal treatment (Figure 7c), and matches the XRD peak at $2\theta = 7.6°$. These results strongly suggest the presence of zeolite beta-like periodic structure in the XRD-amorphous product (72 h). Overall, the structural evolution of aluminosilicates formed
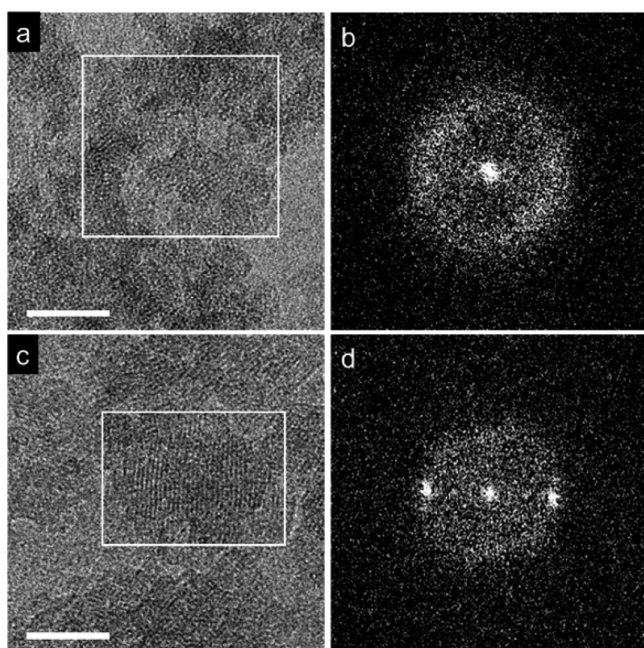
Figure 7. (a, c) High-resolution TEM images and (b, d) the corresponding fast Fourier transforms of the marked areas (white frame) of the products synthesized for 76 (a, b) and 82 h (c, d) (scale bar: 20 nm).

before the onset of crystallization, tracked by combined characterization techniques described above, suggests that the formation of zeolite beta nuclei presumably proceeds by solid-state reorganization of aluminosilicates.

Chemical and Textural Evolution. Chemical compositions of the solid products synthesized for different periods of time are summarized in Table 1. The major notable alteration occurred during the first 24 h of hydrothermal treatment. A drastic decrease in the Si/Al molar ratio was due to the changes in Si and Al yields, corresponding to the dissolution of silica and the following co-condensation of silicate and aluminate. Significant amounts of TEA$^+$ and H$_2$O were occluded in the solid product at this stage, indicating the formation of hydrated, amorphous TEA$^+$–aluminosilicate composites. Further hydrothermal treatment up to 72 h caused slow changes in the chemical compositions of the products, additionally supporting the gradual changes in the structure of the TEA$^+$–aluminosilicate composite during the induction period. The decreases in the amount of water suggest the release of water molecules upon hydrothermal treatment. Both Si and Al solid yields increased in this period (24−72 h) due to the progress of condensation of aluminosilicate species (as also suggested by

solid-state MAS NMR results). It is worth noting that the TEA$^+$/Al molar ratios were almost constant, evidencing the balanced incorporation of TEA$^+$ and Al into the solid products.[25,38]

Other marked changes in the compositions were observed in the product synthesized for 72 and 96 h, where zeolite beta crystals began to be detectable by XRD. Upon crystallization, Al yields decreased, while Si yields increased, causing rapid elevation of the Si/Al ratio, implying that the formation of zeolite beta nuclei leads to the release of Al species from the solid phase or vice versa. This suggestion is also in line with HEXTS results, in which a decrease in the fraction of 4Rs was observed, as it is reported that a higher Al content is preferable for the formation of smaller aluminosilicate rings, that is, 4Rs.[41] The TEA$^+$/Al ratio increased from 1.13 to 1.39, breaking the balanced incorporation of TEA$^+$ and Al. The remaining cationic charges of TEA$^+$ due to the release of Al can be balanced by the framework defects ($\equiv$Si−O$^-$···HOSi$\equiv$).[38] The TEA$^+$/u.c. value of 6.13 was achieved, in agreement with the previous reports that six TEA$^+$ are occluded in a unit cell of zeolite beta over a wide range of Si/Al ratios.[24,25,38] The amount of occluded H$_2$O decreased significantly at this stage, providing a closer contact between TEA$^+$ and aluminosilicate frameworks. Further hydrothermal treatment up to 240 h resulted in a higher solid yield while retaining a constant amount of TEA$^+$ per unit cell.

Argon adsorption−desorption measurements were conducted to track the textural changes in aluminosilicates throughout the synthesis. Adsorption−desorption isotherms in a normal scale are shown in Figure S8 in the SI, while those plotted in a semilog scale are depicted in Figure 8. The presence of mesopores was observable after heating for 24 h, as there were clear uptakes at relative pressure higher than 0.5 with hysteresis loops (Figure S8; SI). The mesoporosity observed for the products after 24−76 h of hydrothermal treatment can be assigned to the interparticular voids of nanoparticles of about 10 nm in diameter observed by FE-SEM. With increased synthesis time (80−240 h), the hysteresis loops due to mesopores gradually diminished, while the sharp uptakes at low relative pressure, a characteristic of micropores, increased. The decreases in mesoporosity during the course of hydrothermal treatment can be explained by the increases in particle sizes, as shown by FE-SEM, after the formation of zeolite beta.

The semilog isotherms (Figure 8) enable us to focus on the uptakes in the micropore range. The product before hydrothermal treatment (0 h) did not have an uptake at $P/P_0 = 10^{-5}−10^{-3}$, indicating the absence of micropores. Gradual uptakes in this range of relative pressures were observed in the

Table 1. Solid Yields and Chemical Compositions of the Products Synthesized for Different Periods of Time[a]

synthesis time (h)	solid yield (wt %)[b]	Si yield (wt %)	Al yield (wt %)	Si/Al	TEA$^+$/u.c.[c]	TEA$^+$/Al	H$_2$O/u.c.[c]	H$_2$O/TEA$^+$
0	82.7	87.0	23.0	79.1	0.941	1.18	3.35	3.56
24	36.4	35.7	73.9	10.1	6.61	1.14	32.8	4.97
48	38.2	37.3	78.9	10.1	6.50	1.13	25.8	3.96
72	40.3	39.6	79.9	10.6	6.21	1.13	24.3	3.91
96	45.0	44.8	71.8	13.6	6.13	1.39	8.29	1.35
240	53.7	53.7	82.3	14.3	6.12	1.46	8.55	1.40

[a]Si and Al contents were quantified by ICP-AES, while TEA$^+$ and H$_2$O amounts were determined by elemental analyses (CHN) and TGA, respectively. [b]Calculated based on oxides (excluding TEA$^+$ and H$_2$O). [c]u.c. stands for a unit cell of the *BEA framework structure consisting of 64 tetrahedral atoms.
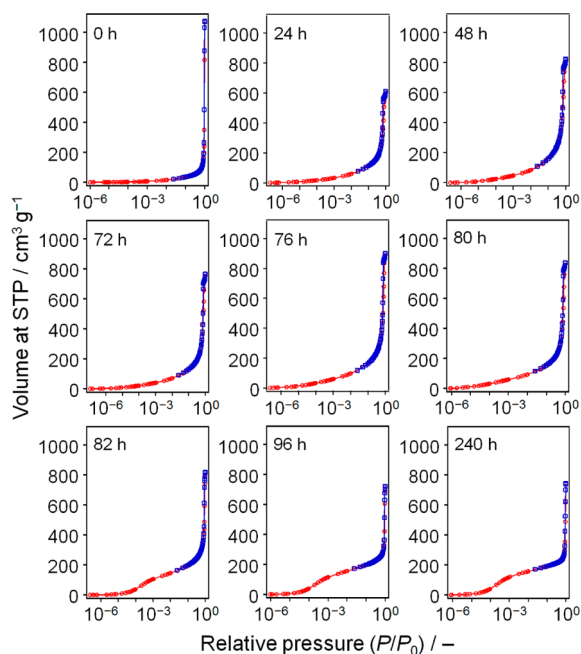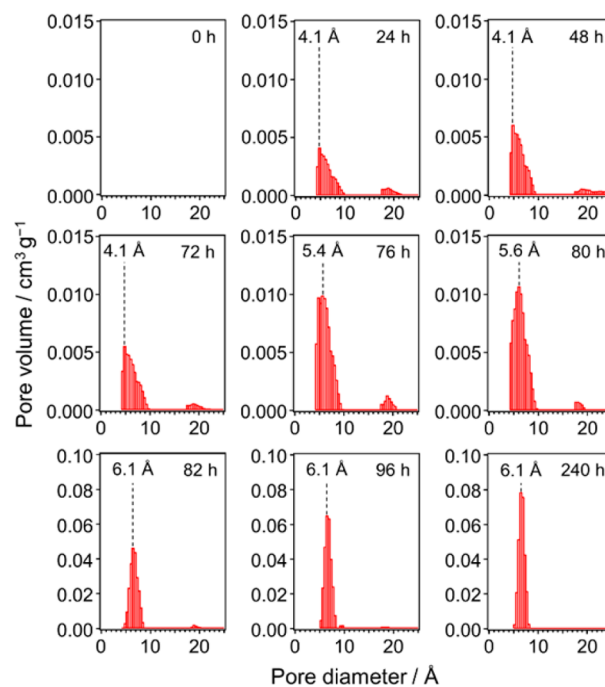
Figure 8. Argon adsorption (in red)−desorption (in blue) isotherms in a semilog scale of the products synthesized for different periods of time.

Figure 9. NLDFT pore size distributions of the products synthesized for different periods of time calculated from isotherms in Figure 8.

24−80 h products and increased as the hydrothermal treatment time was increased, suggesting the formation of micropores with nonuniform distributions. We presume that these micropores are constructed by molecular clusters of TEA⁺ formed during the induction period, in which TEA⁺ functions as pore-fillers.[56] At this stage, still aluminosilicate products were not well ordered. Crystalline products, on the other hand, showed rapid uptakes in this range of relative pressures, reflecting the well-ordered microporous characteristic of zeolites. The formation of uniform micropores with a sudden increase in micropore volume (vide infra) was observed in the products obtained at 80 and 82 h, which agreed well with the sudden increase in crystallinity of the products (see Figure 2a).

Figure 9 shows pore size distributions in the range of micropores estimated by the NLDFT method.[44] No microporosity was present in the product before hydrothermal treatment (0 h). Micropore diameters of the products treated hydrothermally for 24−72 h were less than 4.1 Å (a detectable limit of argon adsorption) and had relatively broad distribution. Then, the micropore diameter started increasing, becoming 5.4, 5.5, and 6.1 Å after 76, 80, and 82 h of hydrothermal treatment, respectively. The pore diameter did not change by further hydrothermal treatment (from 82 to 240 h); however, the micropore size distribution became narrower and sharper. The micropore diameter of 6.1 Å matches well with the diameter of the largest sphere that can diffuse through the micropores of zeolite beta, being 5.95 Å.[57] These results indicate that major textural evolution of aluminosilicates proceeds between 72 and 82 h of hydrothermal treatment.

In the induction period, the incorporation of Al into the silicate frameworks together with the simultaneous occlusion of TEA⁺ into the condensed aluminosilicate networks creates microporous aluminosilicates with gradually evolved frameworks (in terms of aluminosilicate connectivity and ring structures). During the evolution process, it is interesting to look at changes, if any, in the interaction between TEA⁺ and

aluminosilicate frameworks, which can somehow be assessed by TG-DTA measurements. TGA and DTA curves observed under a gas stream of 10% O₂/90% He are shown in Figures S9 (in the SI) and 10a, respectively. After 24 h of hydrothermal treatment, total weight loss increased with the appearance of endothermic and exothermic DTA peaks centered at 60 and 450 °C, respectively. The endothermic peak is attributed to the dehydration of the physically adsorbed water, while the exothermic peak can be assigned to the decomposition of TEA⁺ balancing negatively charged Al sites (≡Si−O⁻−Al≡).[24,25,38] No exothermic peak corresponding to the decomposition of TEA⁺ balancing at framework silanol defects (≡Si−O⁻···HOSi≡), typically appearing at about 360 °C,[24,25,38] was noticeable for the products synthesized for 24−72 h, further verifying the balanced incorporation of TEA⁺ and Al into the solid phase. Because of these balanced charges, it can further be implied that the Al atoms incorporated in the aluminosilicate frameworks are present in the four-coordinated environment. After zeolite beta crystallized, the exothermic DTA peak due to the decomposition of TEA⁺ balancing at framework silanol defects slightly appeared as broad humps at 355 °C in the products obtained after 82−240 h. Note that this exothermic peak is generally unobserved when the Si/Al ratio of zeolite beta is close to 10, that is, about 6 Al/u.c., while it become clearly noticeable at higher Si/Al ratios.[38]

As can be seen in Figure 10b, the peak positions of the exothermic peaks corresponding to the decomposition of TEA⁺ that balances with Al sites slowly shifted toward higher temperature. The decomposition temperature gradually increased to around 450 °C during the induction period and then drastically increased up to above 460 °C upon the crystallization of zeolite beta, revealing the strengthened interaction between TEA⁺ and framework Al sites. The TGA weight losses and the DTA signals became sharper, suggesting the enhanced uniformity of the TEA⁺−aluminosilicate interaction.
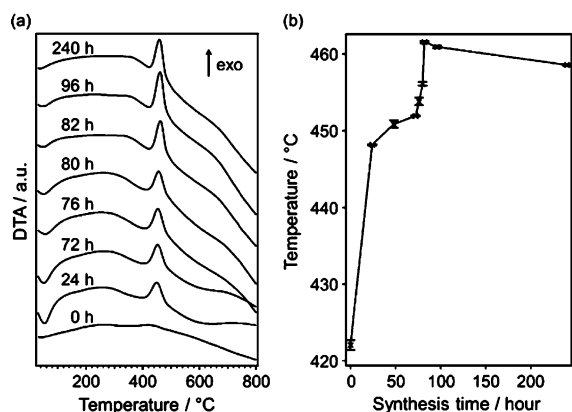
Figure 10. (a) DTA curves of the products synthesized for different periods of time and (b) temperatures at the top of the exothermic peaks seen in the DTA curves. The values plotted in (b) were averaged from three independent measurements.

Although ^{13}C MAS NMR is often employed to characterize the OSDAs occluded in zeolites, useful information on the conformational structures of TEA$^+$ cannot be obtained by a conventional NMR technique, as its conformers are hardly distinguished.[58,59] Instead, Raman spectroscopy allows us to know the steric conformations of TEA$^+$ occluded intact in the aluminosilicate frameworks. A Raman band due to the C_4N symmetric stretching mode of TEA$^+$ can be seen at around 670 cm^{-1}. Two stable TEA$^+$ conformers are observed in an aqueous solution, being *tt.tt* (all-*trans*, D_{2d}) and *tg.tg* (*trans-gauche*, S_4).[60−62] Raman bands at 620−720 cm^{-1} of the products are depicted in Figure S10 in the SI. The deconvolution of Raman bands using Gaussian functions clearly revealed the presence of two distinguishable bands centered at 661 and 673 cm^{-1}, assigned to *tg.tg* and *tt.tt* conformers, respectively.[60−62] Area fractions of two Raman bands attributed to *tt.tt* and *tg.tg* steric conformations along with the synthesis time are plotted in Figure 11. Before hydrothermal treatment (0 h), TEA$^+$ had
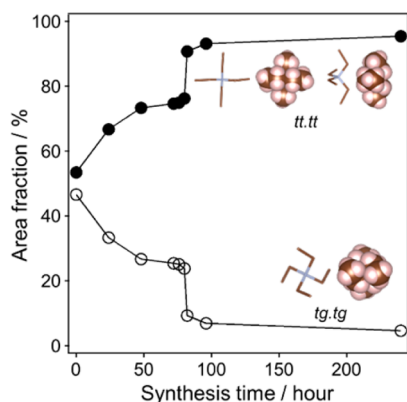
**Figure 11.** Area fractions of *tt.tt* and *tg.tg* conformers of TEA$^+$ derived from Raman spectra.

approximately equivalent amounts of *tt.tt* and *tg.tg* conformers. The fraction of the *tt.tt* conformer then increased upon hydrothermal treatment up to about 75% before the onset of crystallization. The *tt.tt* fraction further increased rapidly with the appearance of zeolite beta, reaching about 95%, indicating that most of the TEA$^+$ present in zeolite beta possesses the *tt.tt* conformation. It is noteworthy that the structure-directing

effects of TEA$^+$ conformers in the formation of (metallo)-aluminophosphate zeotype materials have also been observed previously,[63] in which the conformational changes have been suggested to occur to fit TEA$^+$ in the zeolite cavities by minimizing unoccupied free space and simultaneously to maximize the interaction with substituted metal atoms (i.e., Zn). However, the direct comparison between the aluminosilicate zeolite beta presented here and the previously reported (metallo)aluminophosphates is not so straightforward because of the differences in zeolite framework structures, having different pore dimensions and volumes, and in the chemistry of silicate and phosphate. In addition, in the previous report,[63] the occluded TEA$^+$ is not in a clustered mode, which is completely different from the present case of zeolite beta.

Figures 12a and b show the *tt.tt* fraction of TEA$^+$ plotted with micropore volumes and decomposition temperatures of TEA$^+$
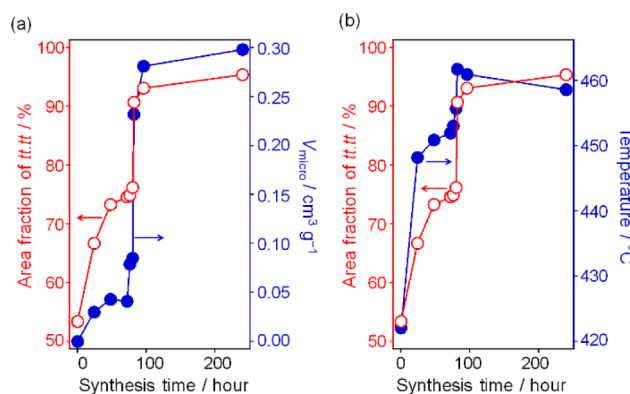
Figure 12. Area fraction of the *tt.tt* conformer of TEA$^+$ derived from Raman spectra plotted with (a) micropore volume and (b) decomposition temperature of TEA$^+$.

stabilized at the framework Al sites, respectively. Up to 72 h of hydrothermal treatment, the micropore volumes increased slowly, indicating gradual evolution of the TEA$^+$−aluminosilicate composites during the induction period. Dramatic increases in the micropore volumes were then observed between 72 and 96 h of hydrothermal treatment, indicating that most of the accessible micropores are formed simultaneously with the formation of zeolite beta. Very interestingly, the fraction of the *tt.tt* conformer of TEA$^+$ and the decomposition temperature of TEA$^+$ stabilized at framework Al sites changed in the same manner as the micropore volumes, suggesting the strong relationship between the formation of micropores and the local structure of TEA$^+$ accompanied by the incorporated Al atoms. We thus postulate that the formation of micropores during the formation of zeolite beta is induced by the TEA$^+$ clusters that reorganize by adapting their conformation into *tt.tt* to enhance the TEA$^+$−aluminosilicate interaction. This can further be supported by considering the geometry of the *tt.tt* and *tg.tg* conformers. As illustrated in Figure 11, the *tt.tt* conformer has an anisotropic, disk-like shape, while the *tg.tg* conformer is an isotropic tetrahedron. The interaction between positive charges at the nitrogen of TEA$^+$ and negative charges at oxygen atoms surrounding the incorporated Al in the aluminosilicate frameworks can be enhanced by shortening the atomic distances between nitrogen and oxygen. In this sense, although the tetrahedral *tg.tg* conformer can provide isotropic interactions with the aluminosilicate frameworks uniformly, the shortest distance

14540

Scheme 1. Proposed Comprehensive Scheme for the Formation of Zeolite Beta Directed by TEA$^+$ in a *Clustered* Structure-Direction Mode^a
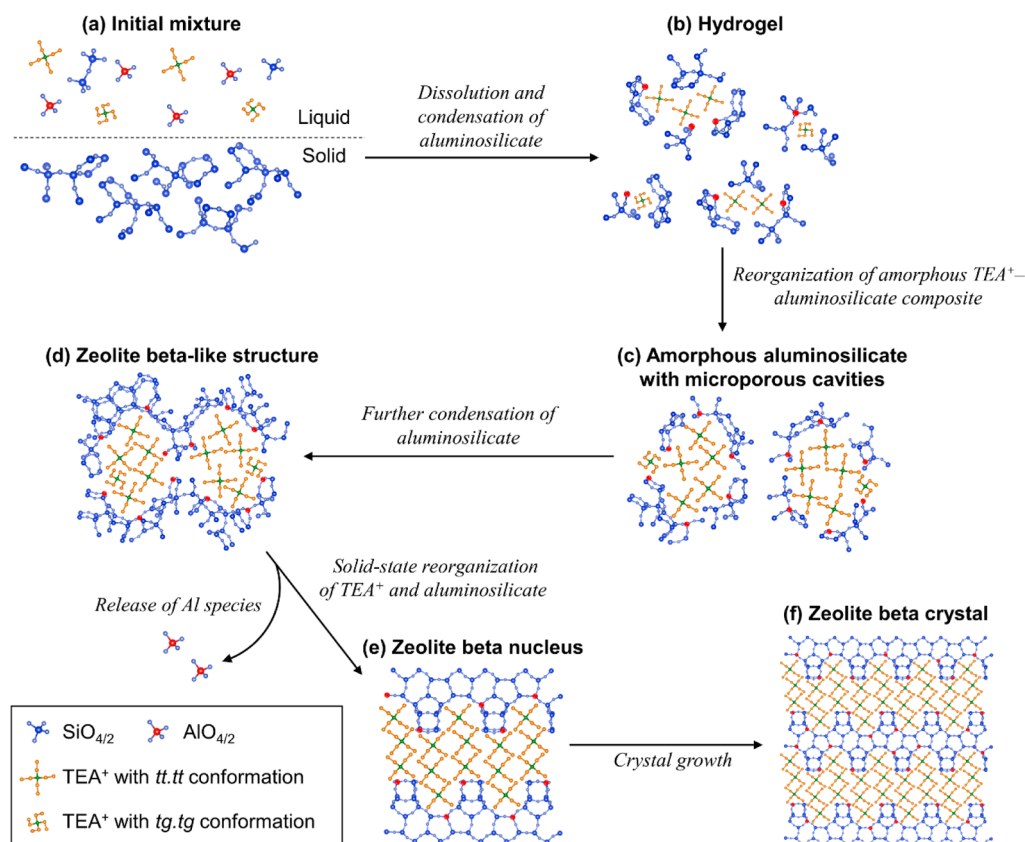
^{a}Both liquid and solid phases are illustrated in (a), while only the solid phase is shown in (b)−(f). Water molecules and hydroxyl anions are omitted for clarity.

between TEA$^+$ and the aluminosilicate frameworks can be achieved only with the disk-shaped *tt.tt* conformer. During the formation of zeolite beta, reorganization of the TEA$^+$ clusters and the aluminosilicate frameworks should occur simultaneously in order to optimize the interactions between them.

Proposed Comprehensive Scheme for the Formation of Zeolite Beta. On the basis of our observations herein, we propose a comprehensive scheme for the formation of zeolite beta, illustrated in Scheme 1, which is, to the best of our knowledge, the most comprehensive thus far. Initially, most TEA$^+$ and Al species are present in the liquid phase, while Si species exist in the solid phase (Scheme 1a). Dissolution of Si species and subsequent co-condensation to form aluminosilicates occur by hydrothermal treatment, yielding tiny nanoparticles of TEA$^+$−aluminosilicate composites with balanced incorporation of TEA$^+$ and Al species (Scheme 1b).

Upon further hydrothermal treatment, reorganization of the TEA$^+$−aluminosilicate composites gradually proceeds, by which the changes in network connectivity and probably ring structures of aluminosilicate frameworks occur simultaneously with the migration of TEA$^+$ in the composites (Scheme 1c). In addition, micropores are gradually developed at this stage. As micropore volumes and diameters increase during such reorganization, TEA$^+$ cations should migrate inside the composites and form molecular clusters. Interestingly, the fraction of *tt.tt* conformer of TEA$^+$ also gradually increases.

Further condensation of aluminosilicates together with further clustering and rearrangement of TEA$^+$ induce the

formation of the TEA$^+$−aluminosilicate composites possessing a local periodic structure resembling that of zeolite beta (Scheme 1d). It should be emphasized here that the XRD-visible crystals are not yet formed at this stage. The TEA$^+$−aluminosilicate composite with the zeolite beta-like structure then suddenly develops to a zeolite beta nucleus via solid-state reorganization of TEA$^+$ and aluminosilicates (Scheme 1e). Most of the accessible micropores form at this stage, and the fraction of *tt.tt* conformer of TEA$^+$ exceeds 90%. Aluminosilicate ring structures change, accompanied by the release of Al species from the solid phase. Subsequently, zeolite beta grows into larger crystals (Scheme 1f).

In the present work, we have paid much attention to a series of events governing the formation of zeolite beta, in particular, how molecular TEA$^+$ adapts itself into clusters that function as the OSDA in the clustered mode, by tracking the evolution of TEA$^+$−aluminosilicate composites formed during the hydrothermal treatment. On the other hand, the events in the crystal growth, that is, the ones after the appearance of XRD-visible crystals, have been less focused on. It has been evidenced recently that silicalite-1 zeolite grows via a combination of classical and nonclassical mechanisms by the addition of both molecular silicate species and nanoparticle precursors, respectively.[9] We surmise that both growth mechanisms may be valid here. To clarify the dominant growth nutrient, as well as to further examine the structure of the amorphous TEA$^+$−aluminosilicate composites, the intermediate addition of seed crystals experiments was conducted.[64] In this experiment, the
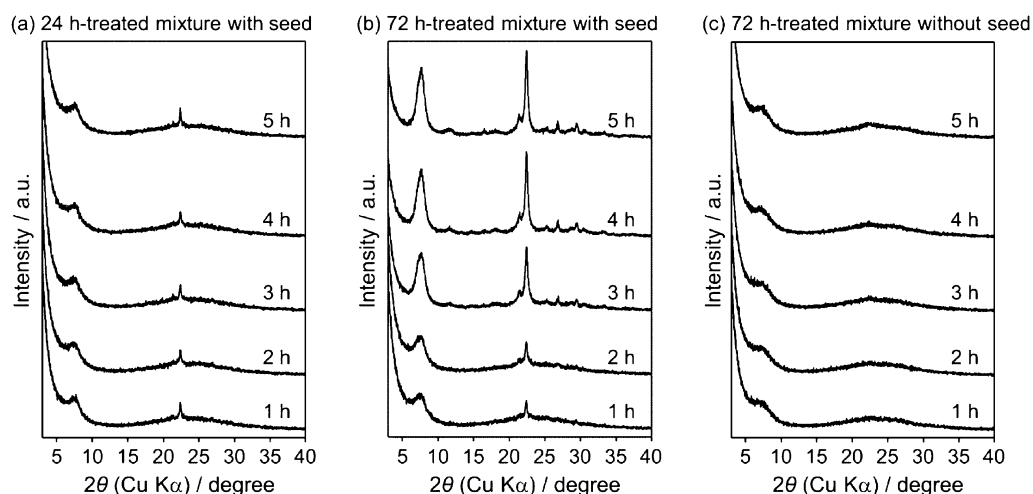
Figure 13. Powder XRD patterns of the products synthesized with (a, b) and without (c) the intermediate addition of seed crystals. Seed crystals were added after (a) 24 and (b) 72 h of hydrothermal treatment of the starting synthesis mixture. (c) Synthesis without the addition of seed crystals by reheating the 72 h hydrothermally treated mixture.

as-synthesized zeolite beta seed crystals were added into the 24 and 72 h hydrothermally treated products, containing both supernatant liquid and precipitated solid. The resulting mixtures were hydrothermally retreated in a tubular reactor with a preheated oil bath, which was used because it can offer faster heat transfer with higher time resolution.[40]

We expect that if the structures of the amorphous TEA^+-aluminosilicate composites treated for 24 and 72 h are similar, the crystallization time required to yield highly crystalline zeolite beta after the addition of seed crystals should be almost the same, regardless of the growth mechanisms. In contrast, if their structures are different, the growth rates should be varied, which can hint at the dominant growth mechanism. If monomers, dimers, and other small oligomers are the major species that take part in the crystal growth, the crystallization time required for the 24 h-treated product should be shorter than that for the 72 h counterpart. This is because the lesser degree of condensation of aluminosilicates after 24 h of treatment makes them dissolve more easily, thereby providing a larger amount of small molecular aluminosilicate species for the crystal growth. On the contrary, if larger precursors are predominant, the crystallization time required for the 72 h-treated product should be shorter, as the 72 h-treated product consists of aluminosilicates with local structures reassembling zeolite beta.

Powder XRD patterns of the products synthesized with and without the addition of the seed crystals are shown in Figure 13. When the seed crystals were added after hydrothermal treatment for 24 h, highly crystalline zeolite beta was not observed even after 5 h of additional hydrothermal treatment (Figure 13a). On the other hand, when the intermediate addition of seed crystals was performed for the synthesis mixture heated for 72 h, the typical XRD pattern of zeolite beta was readily observed after 3 h of additional treatment (Figure 13b). Note that the additional treatment of the 72 h-treated mixture without the addition of seed crystals did not yield zeolite beta (Figure 13c), confirming the effects of seed addition.

Rapid crystallization of zeolite beta occurred when the seed crystals were added after 72 h of hydrothermal treatment of the synthesis mixture, even though the 72 h-treated amorphous aluminosilicate is more condensed, implying that the crystal growth is dominated by precursors larger than molecular aluminosilicate species. In addition, the results obtained from the intermediate addition of seed crystals experiments support that the structure of the amorphous TEA^+-aluminosilicate composite after 72 h of hydrothermal treatment is more similar to zeolite beta than that of the 24 h-treated composite. Although it has been suggested in the case of silicalite-1 zeolite that the primary (or secondary) nanoparticles formed in the early stage of crystallization act as the direct nutrient for the crystal growth by the attachment of such nanoparticles,[7,8] this growth pathway is likely not so straightforward here. Considering the changes in the Si/Al ratio during the crystal growth (96−240 h), the ratio should become lower if the nanoparticles earlier formed supply directly as the growth unit, as they have the lower Si/Al. Rather, crystal growth in the present conditions might follow Ostwald's ripening,[56,65] in which the nanoparticles (i.e., the amorphous TEA^+-aluminosilicate composite) should be dissolved to some extent and release Al before the addition to the surface of zeolite beta as the growth nutrient.

■ CONCLUSIONS

Zeolite beta was synthesized using TEA^+ as an OSDA under hydrothermal conditions in the absence of alkali metal cations, enabling us to successfully track the detailed changes in the structures, chemical compositions and conformation, and textural properties of the TEA^+-aluminosilicate composites formed during the formation of zeolite beta. The structural, chemical, and textural evolution of the composites reveals all the events of the zeolite beta formation and, in particular, the structure-directing behaviors of TEA^+. The most comprehensive scheme for the formation of zeolite beta is proposed as follows: (i) the dissolution of silica and aluminum sources, followed by the co-condensation of aluminosilicates with the simultaneous occlusion of TEA^+ into the solid phase, (ii) the reorganization and further condensation of aluminosilicates together with the migration and conformational rearrangement of TEA^+ within the aluminosilicate networks, resulting in the formation of amorphous TEA^+-aluminosilicate composites having a zeolite beta-like structure, (iii) the formation of zeolite beta nuclei by solid-state reorganization of the zeolite beta-like TEA^+-aluminosilicate composites, accompanied by the release

of Al species from the solid phase, and (iv) the subsequent crystal growth by the addition of aluminosilicates with sizes larger than simple oligomers as the main nutrient.

The crucial step for the crystallization of zeolite beta lies in the induction period, where the TEA$^+$−aluminosilicate composites are gradually transformed into the zeolite beta-like structure, induced by the clustering and conformational rearrangement of TEA$^+$. The conformational rearrangement of TEA$^+$ has a strong relationship with the formation of micropores and the incorporated Al in the aluminosilicate frameworks, revealing that the conformation of TEA$^+$ clusters plays a critical role in the structure direction toward zeolite beta. We anticipate that the results presented here can give a clearer image for the structure direction of OSDAs in the clustered mode and therefore would provide a basis for directing the formation of zeolites in the perspective of engineering the OSDA conformation and the OSDA−aluminosilicate interaction, as well, which may lead to the successful design and synthesis of novel zeolites with unconventional structures and/or compositions.

■ ASSOCIATED CONTENT

Ⓢ Supporting Information

The Supporting Information is available free of charge on the ACS Publications website at DOI: 10.1021/jacs.5b11046.

> Calcination profile of the products for argon adsorption experiments, powder XRD patterns, FT-IR spectrum of TEABr, total structural factors ($S(Q)$), Raman spectra, ring distribution of *BEA zeolite, HR-TEM images, argon sorption isotherms in a normal scale, and TGA curves (PDF)

■ AUTHOR INFORMATION

Corresponding Author

*okubo@chemsys.t.u-tokyo.ac.jp

Present Address

#Quantum Beam Unit, Advanced Key Technologies Division, National Institute for Materials Science, 1-1-1 Kouto, Sayo-cho, Sayo, Hyogo, 679−5148, Japan.

Author Contributions

¶T. Ikuno and W. Chaikittisilp contributed equally to this work.

Notes

The authors declare no competing financial interest.

■ ACKNOWLEDGMENTS

■ REFERENCES

(1) Davis, M. E. *Nature* **2002**, *417*, 813−821.
(2) Cundy, C. S.; Cox, P. A. *Chem. Rev.* **2003**, *103*, 663−701.
(3) Wakihara, T.; Okubo, T. *Chem. Lett.* **2005**, *34*, 276−281.
(4) Čejka, J.; Corma, A.; Zones, S. I. *Zeolites and Catalysis: Synthesis, Reactions and Applications*; Wiley: Weinheim, 2010.
(5) Moliner, M.; Martínez, C.; Corma, A. *Chem. Mater.* **2014**, *26*, 246−258.
(6) Valtchev, V.; Majano, G.; Mintova, S.; Pérez-Ramírez, J. *Chem. Soc. Rev.* **2013**, *42*, 263−290.
(7) Snyder, M. A.; Tsapatsis, M. *Angew. Chem., Int. Ed.* **2007**, *46*, 7560−7573.
(8) Davis, T. M.; Drews, T. O.; Ramanan, H.; He, C.; Dong, J.; Schnablegger, H.; Katsoulakis, M. A.; Kokkoli, E.; McCormick, A. V.; Penn, R. L.; Tsapatsis, M. *Nat. Mater.* **2006**, *5*, 400−408.
(9) Lupulescu, A. I.; Rimer, J. D. *Science* **2014**, *344*, 729−732.
(10) Valtchev, V. P.; Bozhilov, K. N. *J. Am. Chem. Soc.* **2005**, *127*, 16171−16177.
(11) Itani, L.; Liu, Y.; Zhang, W.; Bozhilov, K. N.; Delmotte, L.; Valtchev, V. *J. Am. Chem. Soc.* **2009**, *131*, 10127−10139.
(12) Fan, W.; Ogura, M.; Sankar, G.; Okubo, T. *Chem. Mater.* **2007**, *19*, 1906−1917.
(13) Park, M. B.; Lee, Y.; Zheng, A.; Xiao, F.-S.; Nicholas, C. P.; Lewis, G. J.; Hong, S. B. *J. Am. Chem. Soc.* **2013**, *135*, 2248−2255.
(14) Burkett, S. L.; Davis, M. E. *J. Phys. Chem.* **1994**, *98*, 4647−4653.
(15) Burkett, S. L.; Davis, M. E. *Chem. Mater.* **1995**, *7*, 920−928.
(16) Burkett, S. L.; Davis, M. E. *Chem. Mater.* **1995**, *7*, 1453−1463.
(17) de Moor, P.-P. E. A.; Beelen, T. P. M.; van Santen, R. A. *J. Phys. Chem. B* **1999**, *103*, 1639−1650.
(18) de Moor, P.-P. E. A.; Beelen, T. P. M.; Komanschek, B. U.; Beck, L. W.; Wagner, P.; Davis, M. E.; van Santen, R. A. *Chem. - Eur. J.* **1999**, *5*, 2083−2088.
(19) Mintova, S.; Olson, N. H.; Senker, J.; Bein, T. *Angew. Chem., Int. Ed.* **2002**, *41*, 2558−2561.
(20) Agger, J. R.; Hanif, N.; Cundy, C. S.; Wade, A. P.; Dennison, S.; Rawlinson, P. A.; Anderson, M. W. *J. Am. Chem. Soc.* **2003**, *125*, 830−839.
(21) Aerts, A.; Follens, L. R. A.; Haouas, M.; Caremans, T. P.; Delsuc, M.-A.; Loppinet, B.; Vermant, J.; Goderis, B.; Taulelle, F.; Martens, J. A.; Kirschhock, C. E. A. *Chem. Mater.* **2007**, *19*, 3448−3454.
(22) Kumar, S.; Wang, Z.; Penn, R. L.; Tsapatsis, M. *J. Am. Chem. Soc.* **2008**, *130*, 17284−17286.
(23) Rivas-Cardona, A.; Shantz, D. F. *J. Phys. Chem. C* **2011**, *115*, 13016−13026.
(24) Matsukata, M.; Ogura, M.; Osaki, T.; Kikuchi, E.; Mitra, A. *Microporous Mesoporous Mater.* **2001**, *48*, 23−29.
(25) Matsukata, M.; Osaki, T.; Ogura, M.; Kikuchi, E. *Microporous Mesoporous Mater.* **2002**, *56*, 1−10.
(26) Inagaki, S.; Nakatsuyama, K.; Saka, Y.; Kikuchi, E.; Kohara, S.; Matsukata, M. *J. Phys. Chem. C* **2007**, *111*, 10285−10293.
(27) Hould, N. D.; Lobo, R. F. *Chem. Mater.* **2008**, *20*, 5807−5815.
(28) Hould, N. D.; Kumar, S.; Tsapatsis, M.; Nikolakis, V.; Lobo, R. F. *Langmuir* **2010**, *26*, 1260−1270.
(29) Hould, N. D.; Foster, A.; Lobo, R. F. *Microporous Mesoporous Mater.* **2011**, *142*, 104−115.
(30) Hould, N.; Haouas, M.; Nikolakis, V.; Taulelle, F.; Lobo, R. *Chem. Mater.* **2012**, *24*, 3621−3632.
(31) Lobo, R. F.; Zones, S. I.; Davis, M. E. *J. Inclusion Phenom. Mol. Recognit. Chem.* **1995**, *21*, 47−78.
(32) Kubota, Y.; Helmkamp, M. M.; Zones, S. I.; Davis, M. E. *Microporous Mater.* **1996**, *6*, 213−229.
(33) Moliner, M.; Rey, F.; Corma, A. *Angew. Chem., Int. Ed.* **2013**, *52*, 13880−13889.
(34) Chao, K.-J.; Lin, J.-C.; Wang, Y.; Lee, G. H. *Zeolites* **1986**, *6*, 35−38.
(35) Burton, A. W. *J. Am. Chem. Soc.* **2007**, *129*, 7627−7637.
(36) Pophale, R.; Daeyaert, F.; Deem, M. W. *J. Mater. Chem. A* **2013**, *1*, 6750−6760.

(37) Pulido, A.; Moliner, M.; Corma, A. *J. Phys. Chem. C* **2015**, *119*, 7711−7720.

(38) Chaikittisilp, W.; Yokoi, T.; Okubo, T. *Microporous Mesoporous Mater.* **2008**, *116*, 188−195.

(39) Park, M. B.; Ahn, N. H.; Broach, R. W.; Nicholas, C. P.; Lewis, G. J.; Hong, S. B. *Chem. Mater.* **2015**, *27*, 1574−1582.

(40) Liu, Z.; Wakihara, T.; Oshima, K.; Nishioka, D.; Hotta, Y.; Elangovan, S. P.; Yanaba, Y.; Yoshikawa, T.; Chaikittisilp, W.; Matsuo, T.; Takewaki, T.; Okubo, T. *Angew. Chem., Int. Ed.* **2015**, *54*, 5683−5687.

(41) Wakihara, T.; Kohara, S.; Sankar, G.; Saito, S.; Sanchez-Sanchez, M.; Overweg, A. R.; Fan, W.; Ogura, M.; Okubo, T. *Phys. Chem. Chem. Phys.* **2006**, *8*, 224−227.

(42) Faber, T. E.; Ziman, J. M. *Philos. Mag.* **1965**, *11*, 153−173.

(43) Kohara, S.; Itou, M.; Suzuya, K.; Inamura, Y.; Sakurai, Y.; Ohishi, Y.; Takata, M. *J. Phys.: Condens. Matter* **2007**, *19*, 506101.

(44) Thommes, M.; Mitchell, S.; Pérez-Ramírez, J. *J. Phys. Chem. C* **2012**, *116*, 18816−18823.

(45) Perez-Pariente, J.; Martens, J. A.; Jacobs, P. A. *Appl. Catal.* **1987**, *31*, 35−64.

(46) Chaikittisilp, W.; Sugawara, A.; Shimojima, A.; Okubo, T. *Chem. Mater.* **2010**, *22*, 4841−4843.

(47) Wakihara, T.; Fan, W.; Kohara, S.; Ogura, M.; Sankar, G.; Okubo, T. *Chem. Lett.* **2008**, *37*, 30−31.

(48) Jacobs, P. A.; Beyer, H. K.; Valyon, J. *Zeolites* **1981**, *1*, 161−168.

(49) Jansen, J. C.; van der Gaag, F. J.; van Bekkum, H. *Zeolites* **1984**, *4*, 369−372.

(50) Schoeman, B. J.; Babouchkina, E.; Mintova, S.; Valtchev, V. P.; Sterte, J. *J. Porous Mater.* **2001**, *8*, 13−22.

(51) Mintova, S.; Valtchev, V.; Onfroy, T.; Marichal, C.; Knözinger, H.; Bein, T. *Microporous Mesoporous Mater.* **2006**, *90*, 237−245.

(52) Kobler, J.; Abrevaya, H.; Mintova, S.; Bein, T. *J. Phys. Chem. C* **2008**, *112*, 14274−14280.

(53) Engelhardt, G.; Michel, D. *High-Resolution Solid-State NMR of Silicates and Zeolites*; John Wiley & Sons: New York, 1987.

(54) Han, O. H.; Kim, C.-S.; Hong, S. B. *Angew. Chem., Int. Ed.* **2002**, *41*, 469−472.

(55) Yu, Y.; Xiong, G.; Li, C.; Xiao, F.-S. *Microporous Mesoporous Mater.* **2001**, *46*, 23−34.

(56) Davis, M. E.; Lobo, R. F. *Chem. Mater.* **1992**, *4*, 756−768.

(57) Database of Zeolite Structures, http://www.iza-structure.org/databases/.

(58) Brand, H. V.; Curtiss, L. A.; Iton, L. E.; Trouw, F. R.; Brun, T. O. *J. Phys. Chem.* **1994**, *98*, 1293−1301.

(59) Luzhkov, V. B.; Österberg, F.; Acharya, P.; Chattopadhyaya, J.; Åqvist, J. *Phys. Chem. Chem. Phys.* **2002**, *4*, 4640−4647.

(60) Naudin, C.; Bonhomme, F.; Bruneel, J. L.; Ducasse, L.; Grondin, J.; Lassègues, J. C.; Servant, L. *J. Raman Spectrosc.* **2000**, *31*, 979−985.

(61) Takekiyo, T.; Yoshimura, Y. *J. Phys. Chem. A* **2006**, *110*, 10829−10833.

(62) Goto, T.; Takekiyo, T.; Yoshimura, Y. *J. Phys.: Conf. Ser.* **2008**, *121*, 042005.

(63) O'Brien, M. G.; Beale, A. M.; Catlow, C. R. A.; Weckhuysen, B. M. *J. Am. Chem. Soc.* **2006**, *128*, 11744−11745.

(64) Kamimura, Y.; Tanahashi, S.; Itabashi, K.; Sugawara, A.; Wakihara, T.; Shimojima, A.; Okubo, T. *J. Phys. Chem. C* **2011**, *115*, 744−750.

(65) Cundy, C. S.; Cox, P. A. *Microporous Mesoporous Mater.* **2005**, *82*, 1−78.